Precipitation of greigite and pyrite induced by Thermococcales: an advantage to live in Fe- and S-rich environments?

A. Gorlas, T. Mariotte, L. Morey, C. Truong, S. Bernard, J-M Guigner, J. Oberto, F. Baudin, G. Landrot, C. Baya, et al.

Precipitation of greigite and pyrite induced by Thermococcales: an advantage to live in Fe- and S-rich environments?

A. Gorlas [ID],[1]* T. Mariotte,[1] L. Morey,[1] C. Truong,[2] S. Bernard,[2] J.-M. Guigner,[2] J. Oberto,[1] F. Baudin,[3] G. Landrot,[4] C. Baya,[2] P. Le Pape,[2] G. Morin,[2] P. Forterre[1] and F. Guyot[2,5]

[1]*Université Paris-Saclay, CEA, CNRS, Institute for Integrative Biology of the Cell (I2BC), Gif-sur-Yvette, 91198, France.*

[2]*Institut de Minéralogie, de Physique des Matériaux et de Cosmochimie, UMR 7590 - CNRS, Sorbonne Université, Museum National d'Histoire Naturelle, Paris Cedex 05, 75252, France.*

[3]*Institut des Sciences de la Terre de Paris, UMR 7193 – Sorbonne Université - CNRS, Paris, 75005, France.*

[4]*Synchrotron SOLEIL - SAMBA beamline, Saint-Aubin, 91190, France.*

[5]*Institut Universitaire de France (IUF), Paris, France.*

Summary

Thermococcales, a major order of archaea inhabiting the iron- and sulfur-rich anaerobic parts of hydrothermal deep-sea vents, have been shown to rapidly produce abundant quantities of pyrite FeS_2 in iron–sulfur-rich fluids at 85°C, suggesting that they may contribute to the formation of 'low temperature' FeS_2 in their ecosystem. We show that this process operates in *Thermococcus kodakarensis* only when zero-valent sulfur is directly available as intracellular sulfur vesicles. Whether in the presence or absence of zero-valent sulfur, significant amounts of Fe_3S_4 greigite nanocrystals are formed extracellularly. We also show that mineralization of iron sulfides induces massive cell mortality but that concomitantly with the formation of greigite and/or pyrite, a new generation of cells can grow. This phenomenon is observed for Fe concentrations of 5 mM but not higher suggesting that above a threshold in the iron pulse all cells are lysed. We hypothesize that iron sulfides precipitation

on former cell materials might induce the release of nutrients in the mineralization medium further used by a fraction of surviving non-mineralized cells allowing production of new alive cells. This suggests that biologically induced mineralization of iron-sulfides could be part of a survival strategy employed by Thermococcales to cope with mineralizing high-temperature hydrothermal environments.

Introduction

Iron (Fe) is a cofactor of numerous important cellular processes and hence is an essential nutrient for living organisms (Lasocki *et al*., 2014). Nevertheless, this chemical element can exert severe cell toxicity when present above critical concentrations (Frawley and Fang, 2014). Whereas it occurs at extremely low concentrations, in the nanomolar range, in most oceanic reservoirs (Turekian, 1968), it is found at much higher concentrations (up to ∼25 mM) in one of the most metal-rich biotopes on Earth: the hydrothermal vent environments (e.g. Holden and Adams, 2003; Tivey, 2007; Holden *et al*., 2012; Toner *et al*., 2016). Acidic hydrothermal deep-sea vents, the most biologically active sites in the deep ocean, are sulfur-rich structures characterized by unique physical and chemical properties. The chemical speciations of iron and sulfur at hydrothermal vent environments have been investigated and it has been suggested that they control the habitats of numerous organisms (Luther *et al*., 2001a, 2001b). Whereas in the surrounding aerobic seawater, iron is mainly in ferric form Fe(III) as iron (oxyhydr)oxide minerals, it is predominantly in relatively soluble ferrous form Fe(II) in the anaerobic and reducing hydrothermal fluid (Scholten *et al*., 2019), in which dominant sulfur species are the sulfides S(-II) mainly H_2S, HS^- and lesser S^{2-} (Rickard and Luther, 2007; Gartman *et al*., 2011; Rickard, 2012). In the cooling hydrothermal vent fluid, Fe(II) reacts with S(-II) to form inorganic iron sulfide deposits starting with mackinawite and pyrrhotite (close to an FeS stoichiometry), which are thermodynamically unstable and then evolve mostly into FeS_2 pyrite (Luther, 1991). Significant

efforts have been made to understand the formation process and kinetics of pyrite under laboratory conditions (Benning *et al*., 2000; Rickard & Luther, 2007; Rickard, 2012; Gartman *et al*., 2014; Matamoros-Veloza *et al*., 2018) and it has been demonstrated that greigite (Fe_3S_4) may be a possible intermediate phase in the process of pyrite formation (Hunger and Benning, 2007).

The cycling of iron in hydrothermal sources is not only mediated by geological processes; biological organisms indeed play a role in controlling iron dynamics (Raiswell and Canfield, 2011; Holden *et al*., 2012; Emerson, 2016). It has been shown that microorganisms interact with their mineral environment by promoting mineral dissolution or precipitation. Thus, biologically induced mineralization of Fe is an important process in hydrothermal systems (Holden *et al*., 2012; Zhang *et al*., 2019). For instance, chemolithoautotrophic Fe-oxidizing bacteria (FeOB) such as the mesophile *Mariprofundus ferrooxydans* (Emerson and Moyer, 2002; Emerson *et al*. 2007) are able to oxidize Fe(II) as energy source under microaerophilic conditions. The products of this oxidation consist of Fe(III) oxyhydroxide, in the form of filamentous stalk-like structures allowing the formation of extensive bacterial biofilms Fe-rich on the cool outer surfaces of certain active sulfide chimneys (<100°C) (Emerson *et al*., 2007; Emerson *et al*., 2010; Chan *et al*., 2011; Holden *et al*., 2012; Chan *et al*., 2016). These biogenic minerals, together with abiotic iron oxyhydroxides, could upon heating become interesting substrates for hyperthermophilic Fe(III)-reducing microorganisms (Kashefi and Lovley, 2000; Slobodkin *et al*., 2009; Ver Eecke *et al*., 2009; Emerson *et al*., 2010; Kashefi, 2012; Lin *et al*., 2014; Kashyap *et al*., 2018) such as the archaeon *Geoglobus ahangari* (Kashefi *et al*., 2002). In those cases, cells and iron oxyhydroxides are in close association and the reduction of Fe(III) occurs via mechanisms involving either direct contact with the cells or electron shuttles between the cell and the mineral particles (Manzella *et al*., 2013; Lin *et al*., 2014; Miot and Etique, 2016). The production of iron oxyhydroxides could occur preferentially as microbial communities change from hyperthermophiles to mesophiles, when hydrothermal fluid goes from the inner to the outer side of hydrothermal chimneys and/or during the transition from active to inactive hydrothermal vent (Sylvan *et al*., 2012; Hou *et al*., 2020).

In the interior of active sulfides chimney (>250°C), iron sulfide minerals, mainly pyrite and chalcopyrite, are predominant. The cooler middle layers of the chimneys (typically 80°C–150°C) harbour a population of hyperthermophilic microorganisms, and pyrite and marcasite also arise at these locations, often associated with calcium and magnesium sulfate minerals (Lin *et al*., 2016). The causal relationships existing between

those 'low-temperature' FeS_2 iron di-sulfides and the hyperthermophilic microorganisms inhabiting the chimneys is an open question (Juniper and Fouquet, 1988; McCollom, 2007). As mentioned, sulfate from seawater is abundant in those mixing zones of chimneys and could be thought of as a source of those FeS_2 minerals. Sulfate-reducing bacteria (SRB) are known to produce mackinawite and greigite (Picard *et al*., 2018) and genes of SRB metabolism have been found in the outer walls of chimneys (Kormas *et al*., 2006). So far, however, these microorganisms have not been demonstrated to produce FeS_2 pyrites (Picard *et al*., 2016) and further systematic studies using hyperthermophilic sulfate-reducing bacteria or archaea isolated from hydrothermal chimneys would be necessary to fully test their role. Alternatively, we recently demonstrated that the hyperthermophilic Thermococcales, which are predominant inhabitants of the hot parts of hydrothermal sources (Takai *et al*., 2001; Prieur *et al*., 2004), could be an important contributor to the formation of iron sulfides in their ecosystem (Gorlas *et al*., 2018). To mimic more closely the conditions of a pulse of hydrothermal fluid (Tivey *et al*. 1990) and to study possible biological impact on the formation of iron minerals, Thermococcales cells were incubated with high concentration of dissolved Fe(II) as iron source, a major solute in the hydrothermal fluid (Taylor and Konhauser, 2011). These first mineralization experiments have shown that Thermococcales are able to rapidly produce pyrite (FeS_2) and greigite (Fe_3S_4) within former cells or vesicles and on cellular debris, respectively (Gorlas *et al*., 2018). Cell lysis products are initially loaded with amorphous iron phosphates which provide substrates for greigite nucleation whereas sulfur-rich vesicles (SV) produced by Thermococcales during cell growth (Gorlas *et al*., 2015) evolve mostly into pyrite (Gorlas *et al*., 2018). Members of the order Thermococcales are anaerobes and sulfur reducers using either S(0) or sulfur compounds as electron acceptors thus producing H_2S (Blumentals *et al*., 1990; Adams, 1994; Adams *et al*., 2001; Schut *et al*., 2013); nonetheless, a few Thermococcales species (as *Thermococcus kodakarensis* KOD1) can grow without S(0) and produce H_2 (Kanai *et al*., 2005; Schut *et al*., 2013). As detoxification mechanism, *Thermococcus kodakarensis* is able to produce zero-valent sulfur vesicles (SV) when cultivated in Ravot medium supplemented with elemental sulfur (S(0)) (Gorlas *et al*., 2015). Alternatively, when grown in presence of ʟ-cystine, which contains sulfur at −1 formal oxidation state, *T. kodakarensis* still produces vesicles but which do not contain any zero-valent sulfur in detectable amounts (Gorlas *et al*., 2015).

In order to progress in the mechanistic elucidation of the high-temperature mineralization induced by Thermococcales cells, we have investigated, in the present

study, the mineralization by *Thermococcus kodakarensis* under conditions in which no SVs are produced, i.e. in presence of ʟ-cystine, a condition that was never investigated before. This provided interesting mineralogical comparisons between conditions in which cells are mineralized in presence of zero-valent sulfur (Gorlas *et al*., 2018 and this study) or in presence of ʟ-cystine (this study). Furthermore, we have monitored the biological activity of *T. kodakarensis* under different mineralization conditions, i.e. with or without SVs. This allowed us to propose an original mechanism of survival/adaptation of the population of Thermococcales to strongly mineralizing high-temperature hydrothermal environments.

Results

Effects of S(0) and ʟ-cystine on cell growth and metabolic state

We have analysed growth of *T. kodakarensis* cells in modified Ravot medium, containing 1 g of yeast extract and 1 g of tryptone which provide carbon source and electron donor, in presence of either S(0) or ʟ-cystine. A control without S(0) or ʟ-cystine was performed and no *T. kodakarensis* growth was observed in this condition. Cell growth and metabolic states of cells were monitored in both conditions by cell counting and ATP-metry assays in triplicates (Fig. 1). *T. kodakarensis* shows exponential growth during 6 h in the two media. The growth rate with S(0) as electron acceptor ($0.38 \, h^{-1} \pm 0.019 \, h^{-1}$, black curve in Fig. 1A) was not significantly different from the rate with added ʟ-cystine ($0.36 \, h^{-1} \pm 0.027 \, h^{-1}$, red curve in Fig. 1A). The highest cell concentrations reached in both conditions were 1.5×10^8 cells ml^{-1} after 10 h of growth (Fig. 1A) indicating similar growth kinetics in presence of S(0) or ʟ-cystine. ATP-metry assays indicated an initial intracellular amount of 3.86×10^{-16} mmol ATP/cell in S(0) condition (Fig. 1B) and 1.53×10^{-16} mmol ATP/cell in ʟ-cystine condition before exponential phase begins (Fig. 1C). The highest amounts of ATP/cell were reached after 4 h of growth in both conditions. These values indicated that cells contain on average higher concentrations of ATP during the exponential phase (Fig. 1A–C) than in other physiological states, as already reported for several bacteria (Hironaka *et al*., 2013). Interestingly, the average ATP/cell in S(0) condition ($\sim 2 \times 10^{-13}$ mmol ATP/cell), after 4 h of growth (Fig. 1B), was largely superior and approximately 100 times higher than the one in ʟ-cystine condition (4.7×10^{-15} mmol ATP/cell) (Fig. 1C). When the cells enter in stationary phase, the average amount of ATP/cell decreased and returned to values close to those predating the exponential phase ($\sim 10^{-16}$ mmol ATP/cell) for both conditions (Fig. 1B and C).

Furthermore, the intracellular elemental composition in Thermococcales cells was determined for the elements C, H, N and S after 16 h of growth in presence of S(0) (Supporting Information Fig. S1A) or ʟ-cystine (Supporting Information Fig. S1B). The contents of carbon, hydrogen, nitrogen and sulfur (in weight %) measured in cells growing in S(0) condition were $58.1\% \pm 1.0\%$, $9.2\% \pm 0.2\%$, $16.9\% \pm 0.5\%$ and $15.8\% \pm 1.2\%$, respectively (Supporting Information Fig. S1A.1) whereas in ʟ-cystine condition, they were of $68.4\% \pm 0.5\%$, $11.3\% \pm 0.2\%$ and $20.3\% \pm 0.2\%$ for total carbon, hydrogen and nitrogen, respectively (Supporting Information Fig. S1B.1). In the two growth conditions, the carbon-to-hydrogen ratio (ca 6:1 by weight) and the carbon-to-nitrogen ratio of the samples (ca 3:1 by weight) were similar and close to what is often reported in prokaryotes (Vrede *et al*., 2002). The main difference concerned the presence of intracellular sulfur, which was measured at high level (15.8%) only when cells were cultivated in presence of S(0) (Supporting Information Fig. S1A.1) while *T. kodakarensis* produced sulfur vesicles (Supporting Information Fig. S1A.2) as previously reported (Gorlas *et al*., 2015), whereas no detectable amount of sulfur was identified within cells cultivated in presence of ʟ-cystine (Supporting Information Fig. S1B.1), a condition under which no sulfur vesicles were observed (Supporting Information Fig. S1B.2).

Relationship between the presence of S(0) in the growth medium and pyrite formation

The present study has been intended to further explore the consequences of the two sources of sulfur (S(0) or ʟ-cystine) in terms of biologically induced mineralization. After Thermococcales growth in modified Ravot medium supplemented with either α-sulfur (S(0)) or ʟ-cystine, cells in early stationary phase were incubated with an anoxic solution of ferrous sulfate (5 mM of FeSO$_4$) as iron source at 85°C. In all experiments, sodium sulfide (Na$_2$S) was used to maintain reducing conditions in the medium. In parallel, abiotic controls (without cells) were incubated with FeSO$_4$ solution (5 mM). We report here the mineralogical analyses of the mineralized samples and the characterization of iron sulfide minerals produced by *Thermococcus kodakarensis*, for both conditions at different mineralization times, determined using scanning and transmission electron microscopies, energy dispersive X-ray (EDX) analyses and synchrotron-based X-ray absorption near edge structure spectroscopy (XANES) at the Fe *K*-edge.

In the case of cells grown in presence of S(0), after 24 h of incubation in mineralization medium (short-term experiments) at 85°C, amorphous or poorly ordered FeS was the dominant phase as shown by XANES
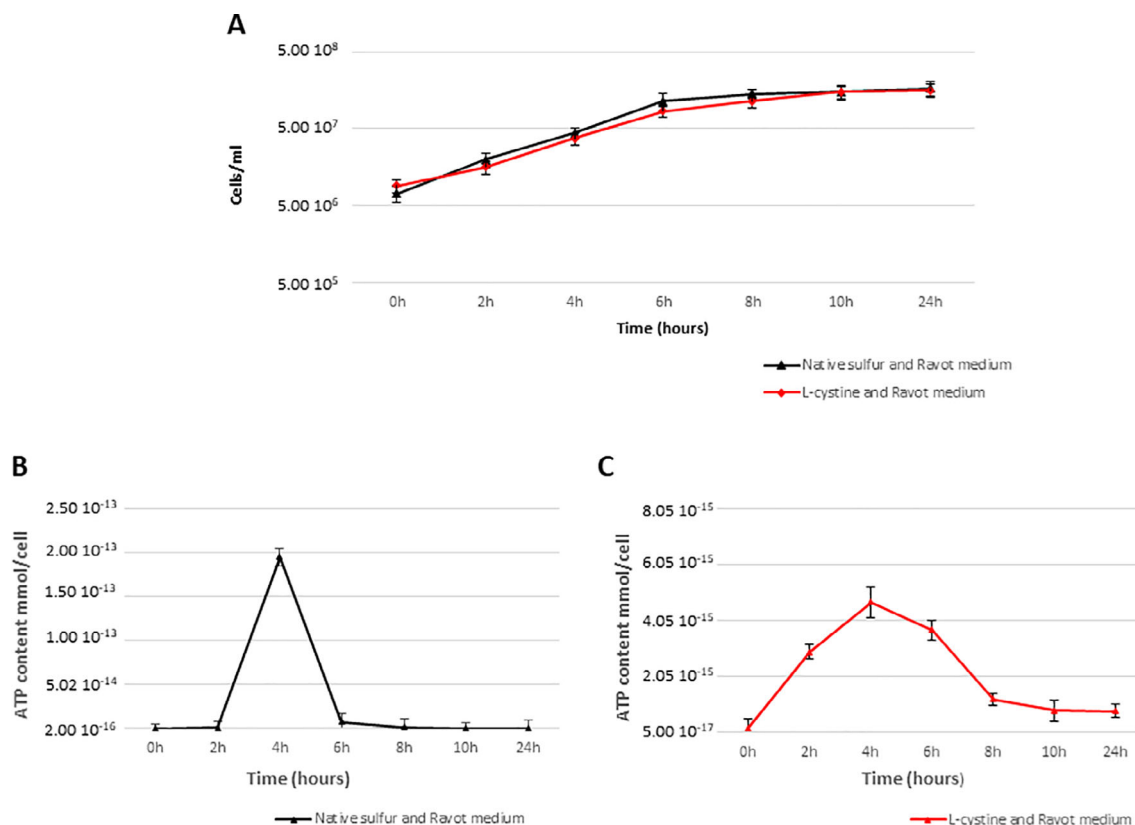
Fig. 1. *T. kodakarensis* cells growth (A) and ATP content (B, C) when cells were grown in the presence of native sulfur (black curves) or in the presence of L-cystine (red curves).

(85% $\pm$ 2%) (Fig. 2C, Table 1). Iron phosphates modelled as vivianite [Fe(II) endmember, 8% $\pm$ 2%] and amorphous iron phosphates [Fe(III) endmember, 11% $\pm$ 2%] were identified. Amorphous iron phosphates were always closely associated with cells as previously described by Gorlas *et al*. (2018). In long-term experiments (after 144 h of incubation in mineralization medium), we observed aggregated spherules cemented together by a matrix containing numerous euhedral nanocrystals (Supporting Information Fig. S2A and B) both composed of iron and sulfur (Supporting Information Fig. S2C, sulfur and iron panels). As verified here by selected area electron diffraction (SAED) in transmission electron microscopy (TEM), the spherules contained FeS$_2$ pyrite (Supporting Information Fig. S3) and were sometimes associated with S(0) as previously described by Gorlas *et al*. (2018). The nanocrystals located on cellular debris and produced in the immediate vicinity of cells and vesicles, were Fe$_3$S$_4$ greigite (indicated by red arrows in the Supporting Information Fig. S2A and B) as previously identified in the study by Gorlas *et al*. (2018). Spherules and matrix accumulated to constitute an entirely mineralized iron and sulfur-rich (Supporting Information Fig. S2C), three-dimensional (3D) structure that

displayed interstitial voids (Supporting Information Fig. S2A). The presence of FeS$_2$ pyrite (Supporting Information Fig. S3) was detected within few tens of hours (after 96 h in the study by Gorlas *et al*. 2018) of mineralization in the form of spherules. Considering their size distribution ($\sim$0.4 μm $\pm$ 0.11), they could correspond to former vesicles that were expelled from cells and possibly to former entire cells, whose size was reduced upon the loss of cytoplasmic materials. After 160 h of incubation in mineralization medium, the cell culture displayed bulk Fe *K*-edge XANES spectra indicating, by linear combination fitting (LCF) analysis, contributions of FeS$_2$ pyrite (49% $\pm$ 13%) and Fe$_3$S$_4$ greigite (41% $\pm$ 9%). A small remaining proportion of FeS (11 $\pm$ 14%) was also present (Fig. 2D, Table 1).

In the case of cells grown in presence of L-cystine, after 5 h of incubation in mineralization medium at 85°C, scanning transmission electron microscopy (STEM) showed that cells or former cells were surrounded by a matrix mainly composed of iron, carbon, phosphorous and oxygen (Supporting Information Fig. S4A) physically separated from the FeS matrix. According to EDX spectra, the Fe/P elemental ratio in the Fe, P, C, O matrix was close to 1 (Supporting Information Fig. S4B) suggesting that the
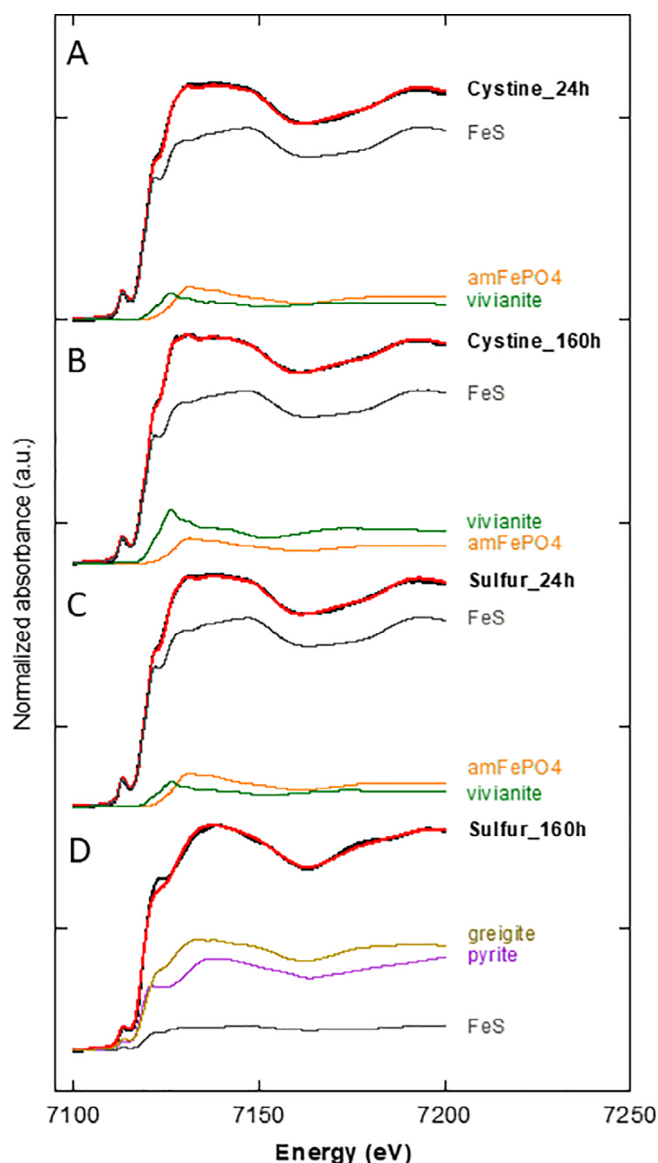
Fig. 2. Normalized Fe *K*-edge XANES spectra for mineralized cells (black lines), grown in the presence of L-cystine (cystine) or S(0) (sulfur), and incubated for 24 h (short-term experiments) or 160 h (long-term experiments) in mineralization medium. A linear combination fitting procedure using synthetic reference compounds has been applied (red lines), and weighted contributions of reference species used in the fits are also plotted. Parameters relative to the LCF procedure are listed in Table 1.
A. Fe *K*-edge XANES spectra for mineralized cells grown in the presence of L-cystine incubated for 24 h (A).
B. Fe *K*-edge XANES spectra for mineralized cells grown in the presence of L-cystine incubated for 160 h.
C. Fe *K*-edge XANES spectra for mineralized cells grown in the presence of S(0) incubated for 24 h.
D. Fe *K*-edge XANES spectra for mineralized cells grown in the presence of S(0) incubated for 160 h.

dominant Fe-bearing phase, associated with biological materials and detected at the first stage of biomineralization, is an amorphous iron phosphate. LCF analysis of the iron *K*-edge XANES spectra obtained for the 24 h-mineralized sample showed that amorphous FeS (86% ± 2%) was dominant, together with both Fe(III)- and Fe(II)-bearing iron phosphates (11% ± 1% amFePO4 and 8% ± 2% vivianite) (Fig. 2A, Table 1). We observed after 144 h an abundant, compact and opaque matrix (Fig. 3A) mainly composed of iron and sulfur as revealed by EDX (Fig. 3B) and mostly yielding amorphous or poorly crystallized materials. LCF analysis of the Fe *K*-edge XANES spectra of the 160 h-mineralized sample revealed that the matrix was mainly composed of FeS (78% ± 2%), accompanied by a mix of Fe(II)- and Fe(III)-iron phosphates, containing this time more Fe(II) (16% ± 1% vivianite and 8% ± 1% amFePO4) (Fig. 2B, Table 1). Cells and vesicles were not observed by TEM, probably because of their weak contrast, whereas some euhedral nanocrystals, easily distinguishable by their cuboidal structure, were observed in the matrix (Fig. 3C). The nanocrystals were clearly visible at boundary edges of the matrix and logically less discernible in depth within the matrix (indicated by red arrows in Fig. 3C). These regular nanocrystals (Fig. 3D) of c.a. 70 nm in size were characterized by electron diffraction (Fig. 3E and F) as Fe_3S_4 greigite. Pyrite was not detected in those samples. Whereas Fe_3S_4 greigite nanocrystals were unambiguously identified by electron diffraction, they were not detected by Fe *K*-edge XANES analysis, probably because of their low abundance (typical detection limit of 5% for XANES) within the FeS matrix (Fig. 2B, Table 1). Few non-mineralized single cells (indicated by black circle in the Supporting Information Fig. S5) were observed with scanning electron microscopy (SEM). Those cells are mainly composed of carbon (panel carbon Supporting Information Fig. S5), contain nitrogen (panel nitrogen Supporting Information Fig. S5) and are close but clearly out of the FeS matrix (panel sulfur and iron Supporting Information Fig. S5). The analyses of abiotic controls, containing S(0) or L-cystine, have revealed the presence of FeS amorphous matrix but neither pyrite nor greigite were observed (Supporting Information Fig. S6).

To sum up, the mineral products formed by Thermococcales during the mineralization experiments varied according to the presence of S(0) or L-cystine, used for growth. Minor amounts of iron phosphates were detected, in similar relative amounts, in all experiments except for long-term experiments in presence of S(0) and were associated with biological materials at least at short mineralization times. Amorphous or poorly ordered FeS was the predominant precipitated phase in all experiments except for long mineralization times in S(0) condition where greigite associated with extracellular materials, and pyrite, encrusting former cells or vesicles, became the two major phases. In long time experiments in L-cystine condition, small amounts of greigite were found scattered in the FeS matrix and pyrite was not observed.

Table 1. Results of LCF analysis of Fe *K*-edge XANES data using reference compounds (see Material and Methods).

Sample	FeS %	amFePO$_4$ %	vivianite %	greigite %	pyrite %	Sum	χ^{2_R} 10^{-4}	R$_{factor}$ 10^{-5}
Cystine_24h	86 (2)	11 (1)	8 (2)	-	-	105	11.3	9.5
Cystine_160h	78 (2)	8 (1)	16 (1)	-	-	102	3.7	3.3
Sulfur_24h	85 (2)	11 (2)	8 (2)	-	-	104	7.7	6.7
Sulfur_160h	11 (14)	-	-	41 (9)	49 (13)	101	21.2	19.9

Uncertainties on the reported values are given with 98% confidence interval (see Material and Methods). Fit quality is estimated by a reduced chi-squares and a R-factor (see Material and Methods).
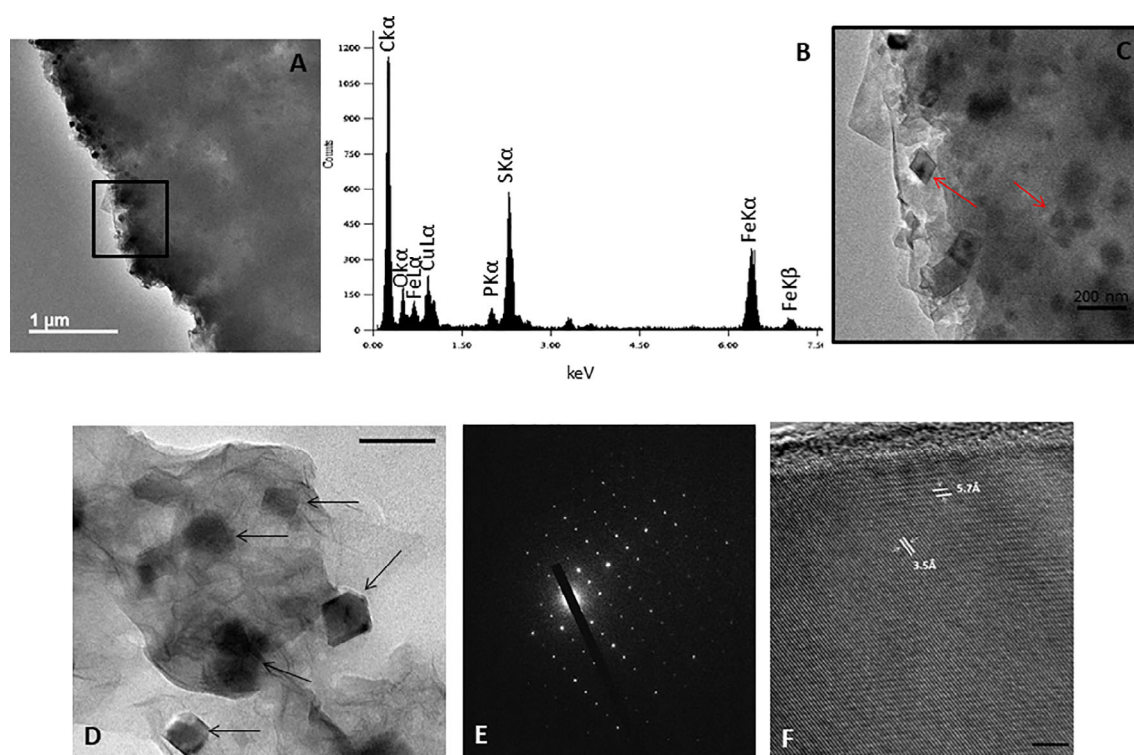

Fig. 3. Production of iron sulfide minerals by *T. kodakarensis* in ʟ-cystine condition after 144 h of incubation in mineralization medium. Transmission electron microscopy image (A, C) of mineralized samples incubated for 144 h with mineralization medium and elemental analysis by EDXS (B). The red arrows indicate the presence of iron sulfide nanocrystals. Transmission electron microscopy image of regular nanocrystals of greigite (indicated by black arrows) disposed on/in the matrix, scale bar = 100 nm (D). Electron diffraction of a greigite nanocrystal (E). High-resolution transmission electron microscopy image of a greigite nanocrystal, scale bar = 5 nm (F).

Restoration of cell growth in long-term mineralization experiments in presence of S(0) in the initial growth medium

The incubation of Thermococcales cells in a medium containing FeSO$_4$ generated rapidly a black precipitate in the flasks (Fig. 4A1) and many black aggregates were observed under optical microscope (Fig. 4A2 and A3). Interestingly, a partial clarification of the medium was observed in long-term mineralization experiments only in S(0) condition (Fig. 4B1). Many motile single cells and dividing cells surrounded the mineralized matrix were then clearly visible under optical microscope (Fig. 4B2 and B3), whereas they were never observed for shorter mineralization times (Fig. 4A3). The observation of dividing cells is a strong evidence confirming the restoration of cell growth in long-term mineralization experiments (Fig. 4B2 and B3). Electron microscopy observations indeed showed non-mineralized cells containing carbon and nitrogen (Fig. 5A) within the iron–sulfur-bearing matrix. More non-mineralized cells were likely present within the mineralized iron sulfide matrix but the contrast due to this mineralized matrix did not allow to identify them. The iron sulfide 3D-structure (Fig. 5B) was mainly composed of pyrite-containing spherules with an intercellular/intervesicular matrix containing greigite nanocrystals (Supporting Information Fig. S7A) as previously described (Gorlas *et al*., 2018). Non-mineralized cells were dispersed and were not affected by iron sulfide mineralization (Fig. 5C, Supporting Information Fig. S7B). To
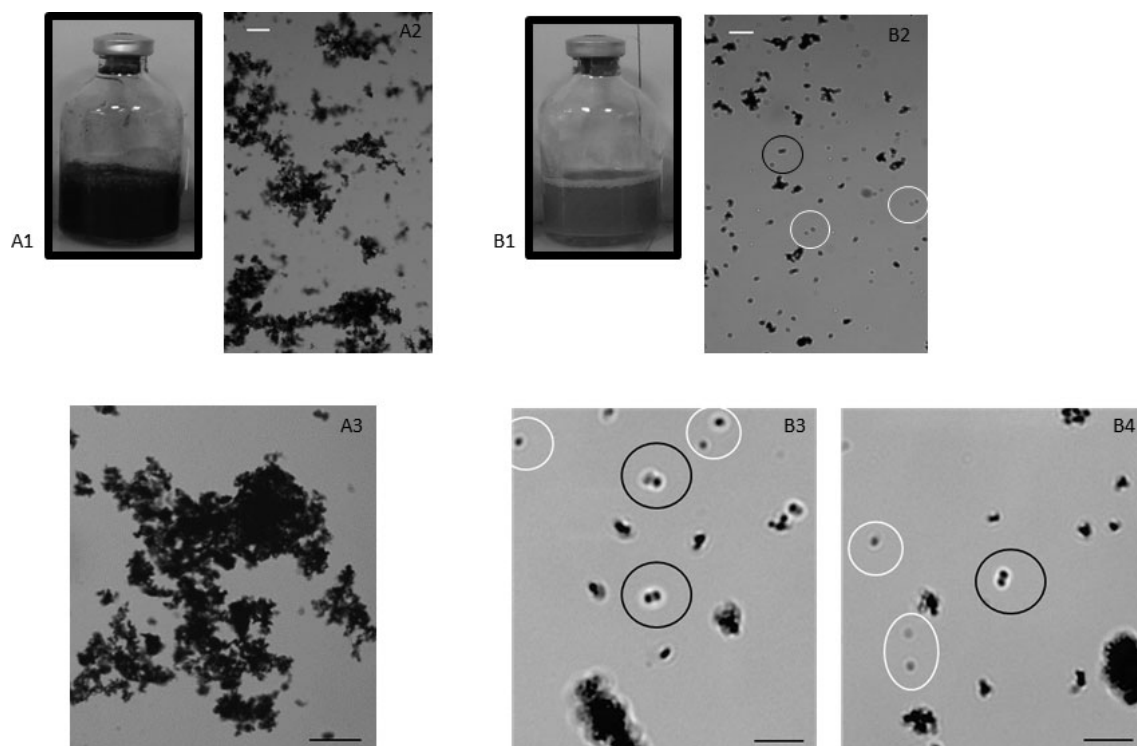
Fig. 4. Observations of mineralization media and cells grown in S(0) incubated after 24 h (A), and 192 h (B) in FeSO₄ solution (5 mM). The incubation of grown cells in FeSO₄ solution rapidly generated black precipitates in the flask (A1). The optical observation shows dense and large black precipitates (A2, scale bar: 10 μm; A3, scale bar: 5 μm). After 192 h of mineralization, the medium is clarified in the flask since it became grey-coloured (B1) and the black precipitates, previously observed, are smaller in size (B2, scale bar: 10 μm; B3, scale bar: 5 μm). The white circles indicate the presence of motile single cell and the black circles indicate the presence of dividing cells.

discount the possibility of contamination, DNA from samples containing this non-mineralized cell population was extracted and sequenced. A BLAST search against the GenBank database revealed 100% of similarity with *Thermococcus kodakaraensis* KOD1 sequence confirming absence of contamination.

ATP concentrations in the mineralizing media were also measured in order to determine the presence of active cells during the mineralization experiments (Fig. 6). The measurements of ATP concentration were consistent with the observations under optical microscope. In S(0) condition (yellow curve in Fig. 6), we observed a rapid decrease of the ATP concentration to undetectable levels within a few minutes after inoculation of cells in the mineralization medium. The ATP concentration then remained undetectable until 96 h of mineralization. Interestingly, after 120 h of incubation in S(0) condition, ATP was again detected in the medium and its concentration gradually increased, to reach a high value of 6.0×10^{-5} mM after 192 h of incubation indicating the presence of metabolically active cells.

In L-cystine conditions, such a restoration of cells population was never observed in the mineralization medium. On the other hand, alive cells persisted in long-term experiments (Supporting Information Fig. S5). The concentration of ATP (blue curve in Fig. 6) in samples decreased progressively to ≈ 0 after incubation of cells in the mineralization medium and remained undetectable in long time experiments (from 120 h to 216 h of incubation in mineralization medium). This suggests that cells remain metabolically active for a while but that metabolic activity is undetectable beyond 120 h of mineralization.

Such late cellular growth was never observed at very high iron concentration in the mineralization medium (as shown, e.g. in S(0) condition with 25 mM of FeSO₄ corresponding to the green curve in Fig. 6). We indeed always observed a rapid and irreversible ATP decrease upon inoculation of cells in mineralization media both in S(0) or L-cystine conditions at iron concentrations of 10, 25 or 50 mM (Supporting Information Fig. S8A and B).

Discussion

Comparison of T. kodakarensis *growth and viability between S(0) and L-cystine conditions*

We have shown that *T. kodakarensis* has equivalent growth rates in modified Ravot medium in presence of
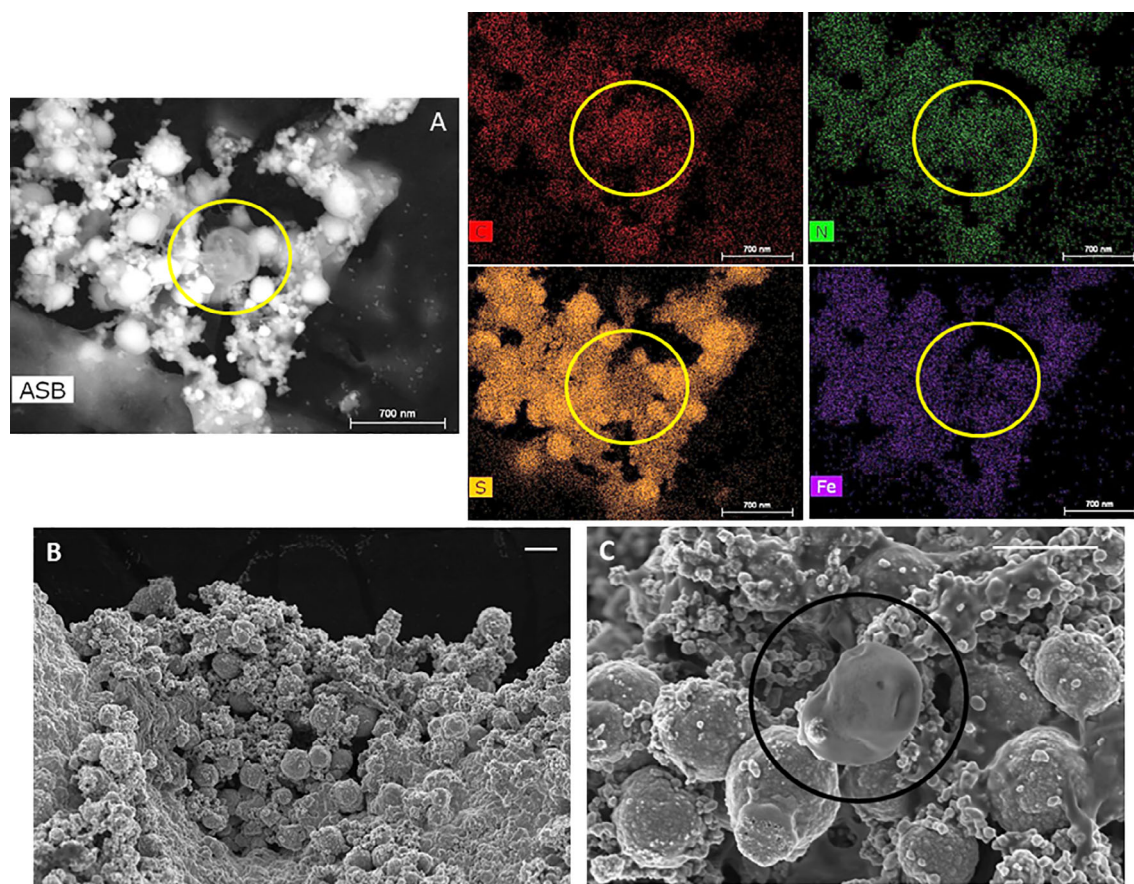
Fig. 5. Presence of living cells after long time experiments in S(0) condition. Scanning transmission electron microscopy of mineralized cells after 192 h of incubation in mineralization medium and associated C (carbon panel), N (nitrogen panel), S (sulfur panel) and Fe (iron panel), scale bar = 700 nm. The yellow circle indicates the presence of non-mineralized cell. SEM images of mineralized and aggregated cells/vesicles incubated for 192 h with mineralization medium. Scale bar = 1 μm. The overall of the mineral-biofilm (A) is mainly composed of pyrite-mineralized cells/vesicles and an intercellular/intervesicular matrix. The black circle indicates the presence of non-mineralized cell which separate itself from the biofilm (B).
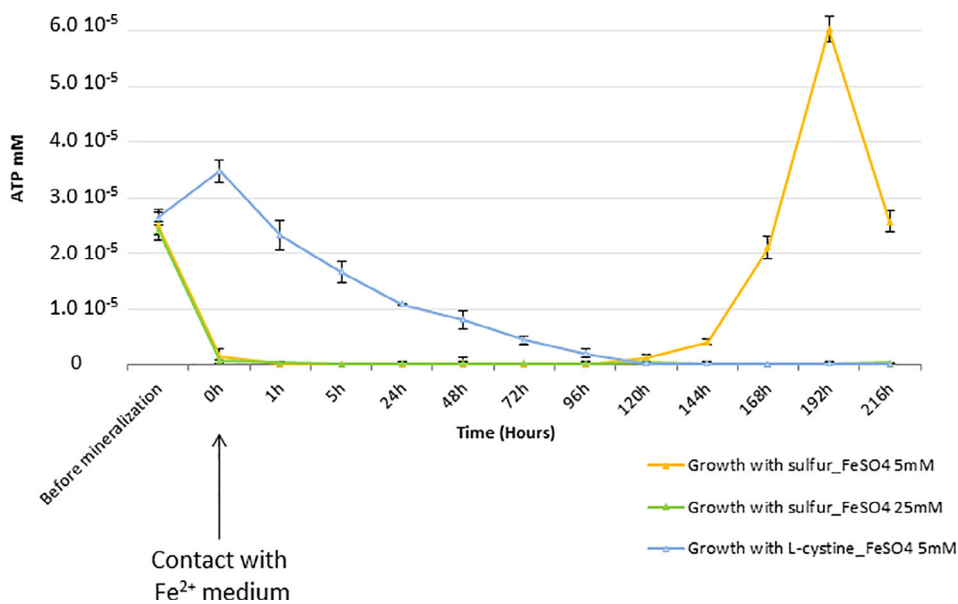
Fig. 6. ATPmetry analyses during biomineralization process. The data represent the ATP content (mM) in the sample when grown cells in L-cystine (blue curve) or in S(0) (yellow curve) are incubated with 5 mM of $FeSO_4$. The green curve represents the ATP level in S(0) condition when cells are incubated with 25 mM of $FeSO_4$.

either S(0) or L-cystine (Fig. 1A). If elemental sulfur S(0) is provided as electron acceptor, respiration of S(0) or fermentation assisted by S(0) explains H_2S formation (Adams *et al*., 2001; Schut *et al*., 2013) as well as abundant precipitation of FeS in the mineralization medium (Gorlas *et al*., 2018 and Fig. 2). Inoculation in a medium containing small amounts of Na_2S (always added to maintain reducing conditions) does not explain significant H_2S formation since we have observed that in the absence of S(0) or L-cystine, no detectable H_2S was formed. In the absence of S(0), *T. kodakarensis* is able to ferment a wide variety of organic compounds mainly peptides and carbohydrates as carbon and energy sources leading to the formation of acetate, CO_2 and H_2. In the L-cystine condition that we investigated, the still detected H_2S and FeS formation might result either from respiration of S(-I) in L-cystine or from fermentation assisted by S(-I) or by H_2-producing fermentation then interacting with L-cystine or initial Na_2S. The kinetics of production of sulfides is obviously much slower in L-cystine than in S(0) condition thus resulting in less rapid iron sulfide mineralization and cell mortality in the former than in the latter condition.

As shown by ATP measurements in rich culture media (Fig. 1B), the metabolic pathways in both conditions result in highly different ATP levels. Interestingly, it has been reported that under a certain level of S(0) in the growth medium, Thermococcales undergo a metabolic shift and thus exclusively produce H_2, whereas with still limited but higher S(0) condition (c.a. 15 mM of elemental sulfur in the medium), Thermococcales are able to simultaneously use both H_2 and S(0) metabolisms (Schut *et al*., 2013). In L-cystine condition (with only ~4 mM of sulfur atoms in the medium), Thermococcales could thus have switched from a sulfur-based metabolism to H_2 production. Even in the case of S(0), one might speculate that after a while, a switch to fermentation may occur. Such a shift in metabolic pathways could explain the smaller concentrations of ATP measured in L-cystine condition than in S(0) condition. Schicho *et al*. (1993) have demonstrated that sulfur respiration is more thermodynamically efficient to produce energy than H_2 production (Schicho *et al*., 1993). This suggests that sulfur respiration mainly occurs when elemental sulfur is present in the growth medium, whereas in the presence of L-cystine, fermentation is the main process employed by *T. kodakarensis*.

Such differences in ATP measurements are further reflected during mineralization incubation. In S(0) condition, the ATP content strongly and immediately decreases when cells are incubated with Fe(II) (Fig. 6). Most cells are rapidly lysed and the cellular material is spread in the medium. In L-cystine condition, ATP decrease is much slower (Fig. 6) suggesting that most living cells are present and decay progressively until ca

100 h. In that case and as suggested by XANES analyses, most cellular materials including phosphates are trapped in a FeS-rich matrix. This matrix is formed in both conditions after inoculation in mineralization medium, as a result of the contact between the H_2S-containing medium and Fe(II) from the mineralization medium, but likely at different rates between the two conditions (Fig. 2, Table 1).

Pyrite mineralization by Thermococcus kodakarensis

Mineralization of pyrite (FeS_2) in connection to the activity of microorganisms has recently been reported in the literature (Gorlas *et al*., 2018; Picard *et al*., 2018; Stanley and Southam, 2018; Thiel *et al*., 2019; Berg *et al*., 2020; Duverger *et al*., 2020) usually requiring quite long incubation times. Here, we show that Thermococcales can indirectly produce FeS_2 pyrite within hours in a simplified synthetic hydrothermal fluid at 85°C, but only when S(0) is present in the initial growth medium. We propose that pyrite mineralization is induced by biological activity of Thermococcales through mediation by biological sulfur vesicles, and probably occurs during or after cell death upon contact between Fe^{2+} and the sulfur vesicles. Although all Thermococcales can use elemental sulfur (S(0)) or L-cystine for yielding H_2S as a by-product (Blumentals *et al*., 1990; Adams *et al*., 2001; Schut *et al*., 2013), the incubation of Thermococcales at pH of ≈ 7 in a Fe(II)- S(-II)-containing medium is not sufficient for producing pyrite (Figs. 2 and 3, Table 1). During cell growth, S(0) (transported as polysulfides or colloidal elemental sulfur) (Schauder and Müller, 1993) is rapidly internalized and stored in Thermococcales cells yielding an high intracellular sulfur concentration (~16% as measured by CHNS in the Supporting Information Fig. S1A). These high sulfur concentrations result in the production of sulfur vesicles, which allow S(0) to be exposed at the surface of the cells (Gorlas *et al*., 2015 and Supporting Information Fig. S1A) and have been interpreted as a sulfur/polysulfide detoxification mechanism (Gorlas *et al*., 2015). In the present study, pyrite was only observed in S(0) experiments where sulfur vesicles were present (Gorlas *et al*., 2015, 2018 and Supporting Information Fig. S1A) and was not observed in L-cystine experiments where sulfur vesicles were absent (Gorlas *et al*., 2015 and Supporting Information Fig. S1B). As previously demonstrated in the study by Gorlas *et al*. (2018), pyrite corresponds closely to the location of the sulfur vesicles. This pyritization process thus occurs in close association with cells and vesicles (Fig. S2). It has been reported that the precipitation of sulfides from hot metal-enriched fluids in hydrothermal chimneys can indeed fossilize organisms, mainly in pyrite, which enables the preservation of organic tissues (Georgieva *et al*., 2015). But these fossils are all from macro-organisms that actually live at lower

temperatures; neither direct nor indirect traces of the hyper-thermophilic biosphere living at temperatures exceeding 80°C have been reported. As shown in the present study, biomineralization of Thermococcales in S(0) condition allows the production of numerous spherules containing pyrites, associated with former intracellular sulfur vesicles. Such spherules might be searched for in hydrothermal chimney samples as possible biosignatures of former Thermococcales cells and vesicles.

Pyrite was never observed in L-cystine experiments, indicating that interaction of Fe(II) with disulfide (S(-I)) from L-cystine did not yield pyrite (Fig. 3). This reinforces the suggestion of an essential role for intracellular S(0) and/or S(0) present in sulfur vesicles for pyrite formation. H_2S, produced by Thermococcales during growth in presence of S(0) or L-cystine, and FeS (Fig. 2, Table 1) could in principle yield pyrite according to the H_2S pathway: $FeS + H_2S \rightarrow FeS_2 + H_2$ (Rickard, 1997; Rickard and Luther, 2007). The experimental results of the present study suggest that the polysulfide pathway: $FeS + S_n^{2-} \rightarrow FeS_2 + S_{n-1}^{2-}$ (Rickard, 1997; Rickard and Luther, 2007) is far more efficient under those conditions than the H_2S pathway for pyrite formation. Although, in strictly anoxic environments, the H_2S pathway will tend to be thermodynamically strongly favoured (Rickard, 1997), the polysulfide pathway may become important in environments with limited but significant oxygen level (Rickard, 1997). Wilkin and Barnes pointed to some conditions where pyrite could be formed from FeS with S(0) but not with H_2S (Wilkin and Barnes, 1996). In our proposed model, we suggest that the production of pyrite is associated with sulfur droplets, and Thermococcales cells are demonstrably a good way to produce such droplets as sulfur vesicles. Then, sulfur vesicles (Supporting Information Fig. S1B) and/or S(0) accumulated in Thermococcales (Supporting Information Fig. S1A) could act as a source of polysulfides and as a precursor for pyrite formation, most likely after cell death. In hydrothermal vents fluids, the presence of polysulfides is very likely (Luther et al., 2001b; Waite et al., 2008; Gartman et al., 2011) and we hypothesize that Thermococcales detoxify them by making S(0) vesicles as they do in the laboratory (Gorlas et al., 2015) thus inducing the low-temperature formation of pyrite in hydrothermal chimneys. Recently, Thiel et al. (2019) have shown that methanogenic archaea are excellent producers of FeS_2 (Thiel et al., 2019). Methanogenic archaea are definitely present in chimney walls (Takai et al., 2001) and their relationships to 'low-temperatures' FeS_2 production in those chimneys deserve further investigations.

Greigite mineralization by Thermococcus kodakarensis

Microbial mineralization of greigite has been known for a long time: whereas magnetotactic bacteria produce it intracellularly (Mann et al., 1990), extracellular greigites have been reported in cultures of sulfate-reducing bacteria (Bertel et al., 2012; Picard et al., 2018; Picard et al., 2019). Biominerals of greigite produced by sulfate-reducing bacteria are detected after several months of incubation in Fe-bearing media (Picard et al., 2019). In the present study, both in S(0) and L-cystine growth media conditions, greigite is produced by Thermococcales within few days (Figs. 2 and 3D–F, Fig. S2, Table 1). In S(0) conditions, greigite is produced where SVs are absent, i.e., on the extracellular materials presumably liberated in the medium by cell lysis in response to FeS precipitation. In L-cystine conditions, where no SVs are available and cell lysis is much less extensive than in S(0) conditions (Supporting Information Fig. S1B; Fig. 6), the mineralization medium is dominated by amorphous or quasi amorphous FeS with only few greigite nanocrystals (Figs. 2 and 3A and B, Table 1). In the study by Gorlas et al. (2018), iron phosphate minerals have been shown to be closely associated with greigite formation. The present study confirms that greigite occurs by sulfurization of amorphous iron phosphates (Supporting Information Fig. S2 for S(0) condition; Fig. 3 and Fig. S4 for L-cystine condition). In both S(0) and L-cystine conditions, greigite nucleation starts outside of cells on cellular debris loaded with iron phosphates (Fig. 2, Table 1, Fig. S4). We suggest that precipitation of greigite on phosphate-loaded cell lysis products might release dissolved phosphates (not measured in this study) in the aqueous phase and presumably other nutriments and molecules. Since greigite precipitation is much more intense in S(0) conditions, release of phosphates could likely more efficient in S(0) than in L-cystine condition. Further studies are required to determine the amount of dissolved phosphates and other molecules during stages of mineralization induced by Thermococcales.

Thermococcales survival strategy in hydrothermal ecosystem

The most remarkable effect observed in the mineralization experiments was the cell revival observed in S(0) condition (Figs. 4–6, Fig. S7). At 5 mM of Fe, we observed the unexpected emergence of T. kodakarensis cells after most cells had been lysed upon initial Fe addition (Figs. 4 and 6). This phenomenon was not observed at higher Fe concentrations suggesting that above a certain iron threshold, all cells were indeed lysed and killed (Fig. S8). The cellular multiplication in a mineralization medium normally not suitable for growth suggests that cells used cellular materials that were made available by cellular lysis. In particular, such a mineralization medium is not suitable to cell growth because of the low solubility of phosphates: dissolved phosphates can abiotically precipitate with Fe(II), preferentially forming Fe(II) phosphates such as vivianite, mainly

dominant in anoxic conditions (Cosmidis *et al*., 2014). This could explain the presence of vivianite identified in shortest time experiments for both conditions and in prolonged time experiments in ʟ-cystine condition (Fig. 2, Table 1). Moreover, precipitation of highly insoluble iron (III) phosphates occurs in the vicinity of cells. The remobilization of phosphates by precipitation of greigites from iron phosphates has recently been reported as an ecological strategy of phosphate recycling in natural environments (Xiong *et al*., 2019; Wilfert *et al*., 2020). The new generation of *Thermococcus kodakarensis* cells appeared after 192 h of mineralization diluting the mineralized phases (Figs. 4 and 5,, Fig. S7), progressive decrease of the FeS matrix for its transformation into pyrite, and possibly dissolving pyrite from the mineralized spherules thus contributing to the partial clarification of the medium (Fig. 4). Pyrite dissolution by iron- and sulfur-oxidizing microorganisms has been reported (Edwards *et al*., 1998; Fowler *et al*., 1999; McGuire *et al*., 2001; Druschel *et al*., 2004). Interestingly, archaea with Fe and/or S assimilatory metabolisms have also been shown to dissolve iron sulfide compounds (Clarkson *et al*., 2021; Payne *et al*., 2021). Mesophilic methanogens are able to catalyse the reductive dissolution of pyrite allowing the liberation of Fe and S, which can be used for cellular biosynthesis (Payne *et al*., 2021). The hyperthermophile *Pyrococcus furiosus* is involved in the dissolution of mackinawite producing FeS complexes, which can then be re-used by *P. furiosus* (Clarkson *et al*., 2021). Further research is needed to identify the exact mechanisms of interactions between iron sulfides and *T. kodakarensis*.

As already observed for other organisms (Little and Vrijenhoek, 2003; Georgieva *et al*., 2015), the elevated initial iron concentrations (here 5 mM in mineralization media) have induced mortality of most of Thermococcales cells. Contrastingly, the cell revival observed in these conditions after few days might indicate a population-scale adaptation to the hydrothermal conditions. The rapid mineralization of cells and vesicles into pyrite within few hours in S(0) condition allows the formation of 3D structures composed of pyrite-mineralized cells/vesicles and an intercellular/intervesicular matrix containing first iron phosphates and FeS and then greigite nanocrystals (Figs. 2 and 5, Table 1, Fig. S2). The formation of greigite in this mineral-biofilm structure is facilitated by the cellular debris, loaded with iron phosphates. These cellular debris are released by cell lysis during the early stages of biomineralization and act as templates for the nucleation of the greigite nanocrystals. We suggest that, during the early stages of mineralization, few non-mineralized cells can be trapped into the informing 3D structure. We speculate that instead of lysis, the non-mineralized Thermococcales cells could enter in quiescent state (i.e. with no metabolic activity). While

those cells cannot divide because they have no access to growth resources, the interior of this mineralized biofilm could present an ecological benefit by protecting the non-mineralized cells against constraints imposed by metal-loaded hydrothermal fluids. Iron minerals in hydrothermal vents are known to scavenge phosphates (Dick *et al*., 2013) that may become a limited nutrient in this ecosystem. Interestingly, some archaeal microorganisms are reported to accumulate polyphosphate into storage granules (Remonsellez *et al*., 2006; Toso *et al*., 2011; Toso *et al*., 2016). Such polyphosphates bodies (PPBs) could help living cells to overcome environmental stresses. It has been suggested that these phosphate-reserves could be employed to resynthesize ATP therefore allowing cells to find new substrates (Toso *et al*., 2011). Whereas we have never observed PPBs within Thermococcales cells, we hypothesize that the amorphous iron phosphates formed during the early stages of mineralization, might efficiently release phosphates upon greigite precipitation. In the S(0) case, the associated release of bioavailable phosphate would be strong enough to allow new cells to grow (Figs. 4–6, Fig. S7). Phosphate release coupled to iron sulfide precipitation has recently been discussed (Xiong *et al*., 2019; Berg *et al*., 2020; Duverger *et al*., 2020; Wilfert *et al*., 2020). Berg *et al*. (2020) demonstrated that pyrite can be produced by sulfate-reducing bacteria (SRB) from Fe(III)phosphate and that this pyritization process is regulated by the SRB activities allowing thus the phosphate release into the aqueous phase. In our study, the released phosphates would be used by the few non-mineralized cells to fuel essential cell functions, including cell division. The absence of cell revival observed in ʟ-cystine conditions over the experimental intervals of this study is in agreement with this model since greigite precipitation is much less efficient in ʟ-cystine conditions than in S(0) experiments and pyrite precipitation is absent (Table 1). However, since precipitation of greigite replacing iron phosphates also occurs in ʟ-cystine experiments, albeit at slower rate, we propose that the cell revival might occur later in time in these conditions.

Conclusion

In this study, we suggest a new mechanism employed by Thermococcales to survive in their harsh environments. We may hypothesize that pulses of hot hydrothermal fluid (i.e. rich in Fe^{2+} and H_2S) common in these environments (Tivey *et al*., 1990; Butterfield *et al*., 1997) in a first round kill most of the cells that then release their phosphate-loaded cellular materials and cell lysis products. Then greigite and pyrite nucleate and grow on those biological materials. In this process, they might release phosphates and organic compounds allowing new cells

to thrive there by fermenting organic matter in presence or in absence of S(0). The diverse metabolic pathways and biologically induced mineralization mechanisms employed by Thermococcales would thus help them to survive in a broad range of extreme environments characterized by the high temperatures and high iron and sulfide contents.

Experimental procedures

Strain, growth and experimental conditions

T. kodakarensis KOD1 (JCM 12380) was cultivated at 85°C with shaking, in modified Ravot medium (contained, per litre of distilled water: 1 g NH_4Cl, 0.2 g $MgCl_2$. $6H_2O$, 0.1 g $CaCl_2$. $2H_2O$, 0.1 g KCl, 0.83 g CH_3COONa. $2H_2O$, 20 g NaCl, 1 g yeast extract, 1 g tryptone, 3.45 g piperazine-*N*,N9-bis (2-ethanesulfonic acid) (PIPES buffer) and 0.001 g resazurin). The pH was adjusted to 7 before autoclaving. After autoclaving, 5 ml of 6% (w/v) K_2HPO_4 and 5 ml of 6% (w/v) KH_2PO4 sterile solutions were added aseptically. The medium was dispensed (50 ml) into 100 ml sterile flasks and supplemented with elemental sulfur (S(0) condition) or L-cystine (L-cystine condition) in separate incubations at 1 g/L. Anaerobiosis was obtained by applying a vacuum to the medium and saturating it with dinitrogen. Finally, a sterile solution of Na_2S. $9H_2O$ [final concentration 0.05% (w/v)] was added to reduce the medium. Growth screening and kinetic experiments were performed in serum bottles in triplicate for each condition. At various time points (0H, 2H, 4H, 6H, 8H, 10H and 24 h), aliquots were collected to determine cell concentration by direct cell counting using a phase-contrast microscope (Olympus) and a modified Thoma chamber. The metabolic state of cells was monitored by using ATP-metry assays. Total and intracellular ATP were monitored using luciferin/luciferase luminescence reaction by using the microbial ATP kit HS (BioThema) and a Kikkoman luminometer. With this method, the luminescence produced is established in relative luminescence units (RLU). Extracellular ATP was directly measured from extracellular medium. Intracellular ATP is measured after using the ATP Eliminating Reagent for degrading extracellular ATP, the extractant BS for making the intracellular ATP accessible to luciferase, the ATP reagent HS containing luciferase/luciferin and an ATP standard. Light is measured before and after adding the ATP standard to calibrate each assay. This compensates for all types of analytical interference (pH, temperature, presence of minerals) (Lundin, 2000). Light measured for controls (without cells) was always inferior to 300 RLU. A baseline value of 300 RLU was always removed to the light value of the samples containing cells.

CHNS elemental analyses

To determine the intracellular elemental composition of cells, *T. kodakarensis* cells were cultivated as previously described. The 10 ml of cells in stationary phase ($2 \cdot 10^8$ cells ml^{-1}) was centrifuged at 5000*g* for 20 min. Pellets of cells were washed three times with 5 ml of TN buffer (10 mM Tris–HCl, 1 mM NaCl). The pellets containing 3 mg of material were dried at 70°C and were kept at −20°C. Samples were analysed by using the elemental analyser Flash 2000 (Thermo Fischer).

Biomineralization experiments

T. kodakarensis cells were grown in modified Ravot medium either in presence of S(0) or L-cystine (as previously described) to reach the early stationary phase, with concentrations of $5 \cdot 10^7$ cells ml^{-1}. Then an anoxic solution of ferrous sulfate ($FeSO_4$) at a final concentration of 5 mM was transferred to grown cells. The modified Ravot medium in presence of $FeSO_4$ is named mineralization medium in this study. In parallel, controls (without cells) were performed in the same conditions as previously described.

Moreover, mineralization experiments were also carried out with higher concentrations of $FeSO_4$ (10, 25 and 50 mM). Cultures and controls were then incubated at 85°C with shaking and were regularly sampled over 216 h. The short-term experiments corresponded to cultures incubated with mineralization medium up to 120 h and the long-time experiments corresponded to cell incubations in the mineralization medium from 120 h to 216 h. The metabolic state of cells during biomineralization experiments was monitored by ATP-metry assays. To determine the composition of the mineralized cells and the mineral end products, we used a combination of SEM, scanning transmission electron microscopy (STEM), TEM, high-resolution transmission electron microscopy (HRTEM), and energy dispersive X-ray spectroscopy analysis (EDXS analysis).

Transmission electron microscopy, high-resolution TEM, scanning transmission electron microscopy and scanning electron microscopy

To prepare samples for TEM, HRTEM and STEM, 2 ml of cultures (at different times of mineralization: 5 h, 144 h and 192 h) was centrifuged at 5000*g* for 20 min. The pellets were washed with 1 ml of TE (10 mM Tris–HCl, 1 mM EDTA) and were centrifuged at 1500*g* for 5 min to remove cellular debris. Supernatants were subsequently centrifuged at 5000*g* for 10 min. The pellets were then resuspended in 200 μl of TE. A 20 μl droplets of samples were adsorbed onto a carbon-coated copper grid for

1 min. After removing the excess liquid, the grids were rinsed with sterile water. To prepare samples for SEM, cells were fixed in 2% glutaraldehyde in TE (10 mM Tris–HCl, 1 mM EDTA) for 4 h at 4°C, washed overnight TE. The cells were then post-fixed for 1 h at room temperature with 1% osmium tetroxide in TE. The cells were dehydrated in a graded ethanol series and dried by critical point drying with a Leica EM CPD300 instrument. For TEM, HRTEM and STEM, specimens were respectively examined using a JEOL JEM-100 CX II, operating at 120 kV and a JEOL JEM-2100F, equipped with a field emission gun (FEG) operating at 200 kV; for SEM, specimens were observed with a Zeiss Gemini 1550VP field-emission scanning electron microscope (Ultra55) equipped with Everhart–Thornley secondary electron detectors, in-lens and backscattered electron detectors.

Cryo-electron microscopy

To prepare samples for Cryo-EM, 10 ml of cultures was centrifuged at 5000g for 20 min. The pellets were resuspended with 50 μl of buffer (10 mM Tris–HCl, 100 mM NaCl, 5 mM CaCl$_2$). The 5 μl droplets of preparations were adsorbed onto a holey carbon-coated TEM support grid (QUANTIFOIL®) typically used for Cryo-EM. After removing the excess liquid with Whatman® paper, the grids were quickly immersed in liquid ethane and transferred into the microscope using a side entry nitrogen-cooled cryoholder (Gatan, 626-DH cryotransfer system). The observations were performed with a Cryo-EM JEOL 2100 LaB6 TEM with an accelerating voltage of 200 kV, at the nominal magnification of 10 000. Images were recorded under low dose conditions with ultra-scan 1000 camera (Gatan, 2 k × 2 k pixels CCD).

Energy dispersive x-ray spectroscopy analysis

EDXS (JEOL, resolution: 140 eV/channel) was carried out to detect compounds that were either adsorbed to the cell surface or entrapped in the vesicles. EDXS analyses have been coupled with TEM and Cryo-EM.

X-ray absorption near-edge structure spectroscopy at the Fe K-edge

Fe K-edge X-ray absorption spectra of the biotic samples were collected at 20 K in transmission detection mode on the SAMBA beamline (SOLEIL, Saint-Aubin, France). Incident beam energy was monitored by using a Si(220) double-crystal monochromator, equipped with dynamic sagittal focusing of the second crystal. Samples were prepared by filtering 5 ml of the mineralized archaea cells, grown in presence of S(0) or L-cystine and incubated for 24 h and 160 h in mineralization medium,

through 0.2 μm polycarbonate filters that were then vacuum-dried for 10 min in an evacuator placed in an anoxic Jacomex™glove box (<1 ppm O$_2$) at IMPMC. The dry filters were then folded once and sealed under Kapton™ tape, which yielded absorption edge step height in the range of 0.1–0.3 at the Fe K-edge. Samples were transferred in strictly anoxic vials and mounted on the cryostat sample holder in a similar glove box at SOLEIL. Sample holders when then immediately plunged into a liquid nitrogen-filled Dewar before being inserted into the liquid He cryostat (TBT) for XAS measurements. Data were then collected in continuous quick-scan mode using a scan-speed of 2 eV s^{-1} and a resulting 0.2 eV step.

Bulk iron speciation in the samples was then determined by linear combination least-squares (LC-LS) fitting of the XANES spectra using model compounds spectra selected on the basis of our electron microscopy observations and by comparison with a large database of already published spectra for iron sulfides (Wang *et al*., 2014; Noël *et al*., 2014, 2017; Morin *et al*., 2017; Merrot *et al*., 2019), phosphates (Cosmidis *et al*., 2014; Muehe *et al*., 2016) and oxyhydroxides (Maillot *et al*., 2011; Hohmann *et al*., 2010; Baumgartner *et al*., 2016; Zeyen *et al*., 2019). Best LC-LS fits of the XANES spectra for the biotic samples studied here were obtained using the spectra of the following four model compounds: poorly ordered FeS, pyrite [FeS$_2$], greigite [Fe$_3$S$_4$], amorphous iron phosphate [am-Fe^{III}PO$_4$•nH$_2$O], and vivianite [(Fe$^{II}_3$PO$_4$)$_2$•8H$_2$O]. LC-LS fitting of the XANES spectra was performed using a classical Levenberg–Marquardt minimization algorithm implemented in a custom-built program (Morin *et al*., 2003). According to Ravel and Newville (2005), fit quality was estimated by a R-factor: $Rf = \Sigma\ [\mu_{exp} - \mu_{calc}]^2/\Sigma\ y_{exp}^2$ where μ is the normalized absorbance, and by a reduced chi-squares (χ_R^2). According to Stetten *et al*. (2018) and Seder-Colomina *et al*. (2018), this reduced chi-squares for XANES spectra was calculated as, $\chi_R^2 = N/(N-N_p)\sum[\mu_{exp} - \mu_{calc}]^2$, where N_p is the number of fitting components and N is the number of independent parameters corresponding to the energy range divided by the natural width of the Fe K-level reported by Krause and Oliver (1979). The uncertainty on the fitting components was estimated to 99.7% confidence (3 sigma) by $3 \times \sqrt{\text{VAR}(p)\chi_R^2}$, where VAR(*p*) is the variance of component *p* returned by the minimization routine for the lowest χ_R^2 value (Stetten *et al*., 2018; Seder-Colomina *et al*., 2018).

Acknowledgements

References

Adams, M.W.W. (1994) Biochemical diversity among sulfur-dependent, hyperthermophilic microorganisms. *FEMS Microbiol Rev* **15**: 261–277.

Adams, M.W.W., Holden, J.F., Menon, A.L., Schut, G.J., Grunden, A.M., Hou, C., *et al*. (2001) Key role for sulfur in peptide metabolism and in regulation of three hydrogenases in the hyperthermophilic archaeon Pyrococcus furiosus. *J Bacteriol* **183**: 716–724.

Baumgartner, J., Menguy, N., Gonzalez, T.P., Morin, G., Widdrat, M., and Faivre, D. (2016) Elongated magnetite nanoparticle formation from a solid ferrous precursor in a magnetotactic bacterium. *J R Soc Interface* **13**: 20160665.

Benning, L.G., Wilkin, R.T., and Barnes, H.L. (2000) Reaction pathways in the Fe–S system below 100°C. *Chem Geol* **167**: 25–51.

Berg, J.S., Duverger, A., Cordier, L., Laberty-Robert, C., Guyot, F., and Miot, J. (2020) Rapid pyritization in the presence of a sulfur/sulfate-reducing bacterial consortium. *Sci Rep* **10**: 8264.

Bertel, D., Peck, J., Quick, T.J., and Senko, J.M. (2012) Iron transformations induced by an acid-tolerant Desulfosporosinus species. *Appl Environ Microbiol* **78**: 81–88.

Blumentals, I.I., Itoh, M., Olson, G.J., and Kelly, R.M. (1990) Role of polysulfides in reduction of elemental sulfur by the hyperthermophilic archaebacterium Pyrococcus furiosus. *Appl Environ Microbiol* **56**: 1255–1262.

Butterfield, D.A., Jonasson, I.R., Massoth, G.J., Feely, R.A., Roe, K.K., Embley, R.E., *et al*. (1997) Seafloor eruptions and evolution of hydrothermal fluid chemistry. *Philos Trans Roy Soc London A* **355**: 369–386.

Chan, C.S., Fakra, S.C., Emerson, D., Fleming, E.J., and Edwards, K.J. (2011) Lithotrophic iron-oxidizing bacteria produce organic stalks to control mineral growth: implications for biosignature formation. *ISME J* **5**: 717–727.

Chan, C.S., McAllister, S.M., Leavitt, A.H., Glazer, B.T., Krepski, S.T., and Emerson, D. (2016) The architecture of iron microbial mats reflects the adaptation of chemo-lithotrophic iron oxidation in freshwater and marine environments. *Front Microbiol* **7**: 796.

Clarkson, S.M., Haja, D.K., and Adams, M.W.W. (2021) The hyperthermophilic archaeon Pyrococcus furiosus utilizes environmental iron sulfide cluster complexes as an iron source. *Extremophiles* **25**: 249–256.

Cosmidis, J., Benzerara, K., Morin, G., Busigny, V., Lebeau, O., Othmane, G., *et al*. (2014) Biomineralization of iron-phosphates in the water column of Lake Pavin (Massif Central, France). *Geochim Cosmochim Acta* **126**: 78–96.

Dick, G.J., Anantharaman, K., Baker, B.J., Li, M., Reed, D.C., and Sheik, C.S. (2013) The microbiology of deep-sea hydrothermal vent plumes: ecological and biogeographic linkages to seafloor and water column habitats. *Front Microbiol* **4**: 124.

Duverger, A., Berg, J.S., Busigny, V., Guyot, F., Bernard, S., and Miot, J. (2020) Mechanisms of pyrite formation promoted by sulfate-reducing bacteria in pure culture. *Front Earth Sci* **8**: 588310.

Druschel, G.K., Baker, B.J., Gihring, T.M., and Banfield, J.F. (2004) Acid mine drainage biogeochemistry at iron mountain California. *Geochem Trans* **5**: 13.

Edwards, K.J., Schrenk, M.O., Hamers, R., and Banfield, J.F. (1998) Microbial oxidation of pyrite: experiments using microorganisms from an extreme acidic environment. *Am Miner* **83**: 1444–1453.

Emerson, D., and Moyer, C.L. (2002) Neutrophilic Fe-oxidizing bacteria are abundant at the Loihi seamount hydrothermal vents and play a major role in Fe oxide deposition. *Appl Environ Microbiol* **68**: 3085–3093.

Emerson, D., Rentz, J.A., Lilburn, T.G., Davis, R.E., Aldrich, H., Chan, C., and Moyer, C.L. (2007) A novel lineage of Proteobacteria involved in formation of marine Fe-oxidizing microbial mat communities. *PLoS One* **8**: e667.

Emerson, D., Fleming, E.J., and Mcbeth, J.M. (2010) Iron-oxidizing bacteria: an environmental and genomic perspective. *Annu Rev Microbiol* **64**: 561–583.

Emerson, D. (2016) The irony of iron - biogenic iron oxides as an iron source to the ocean. *Front Microbiol* **6**: 1502.

Fowler, T.A., Holmes, P.R., and Crundwell, F.K. (1999) Mechanism of pyrite dissolution in the presence of Thiobacillus ferrooxidans. *Appl Environ Microbiol* **65**: 2987–2993.

Frawley, E.R., and Fang, F.C. (2014) The ins and outs of bacterial iron metabolism. *Mol Microbiol* **93**: 609–616.

Gartman, A., Yücel, M., Madison, A.S., Chu, D.W., Ma, S., Janzen, C.P., *et al*. (2011) Sulfide oxidation across diffuse flow zones of hydrothermal vents. *Aquat Geochem* **17**: 583–601.

Gartman, A., Findlay, A.J., and Luther, G.W. (2014) Nanoparticulate pyrite and other nanoparticles are a widespread component of hydrothermal vent black smoker emissions. *Chem Geol* **366**: 32–41.

Georgieva, M.N., Little, C.T., Ball, A.D., and Glover, A.G. (2015) Mineralization of Alvinella polychaete tubes at hydrothermal vents. *Geobiology* **13**: 152–169.

Gorlas, A., Marguet, E., Gill, S., Geslin, C., Guigner, J.M., Guyot, F., and Forterre, P. (2015) Sulfur vesicles from Thermococcales: A possible role in sulfur detoxifying mechanisms. *Biochimie* **118**: 356–364.

Gorlas, A., Jacquemot, P., Guigner, J.M., Gill, S., Forterre, P., and Guyot, F. (2018) Greigite nanocrystals produced by hyperthermophilic archaea of Thermococcales order. *PLoS One* **13**: e0201549.

Hironaka, I., Iwase, T., Sugimoto, S., Okuda, K., Tajima, A., Yanaga, K., and Mizunoe, Y. (2013) Glucose triggers ATP secretion from bacteria in a growth-phase-dependent manner. *Appl Environ Microbiol* **79**: 2328–2335.

Hohmann, C., Winkler, E., Morin, G., and Kappler, A. (2010) Anaerobic Fe(II)-oxidizing bacteria show as resistance

and immobilize as during Fe(III) mineral precipitation. *Environ Sci Technol* **44**: 94–101.

Holden, J.F., and Adams, M.W. (2003) Microbe-metal interactions in marine hydrothermal environments. *Curr Opin Chem Biol* **7**: 160–165.

Holden, J.F., Breier, J.A., Rogers, K.L., Schulte, M.D., and Toner, B.M. (2012) Biogeochemical processes at hydrothermal vents: microbes and minerals, bioenergetics, and carbon fluxes. *Oceanography* **25**: 196–208.

Hou, J., Sievert, S.M., Wang, Y., Seewald, J.S., Natarajan, V.P., Wang, F., and Xiao, X. (2020) Microbial succession during the transition from active to inactive stages of deep-sea hydrothermal vent sulfide chimneys. *Microbiome* **8**: 102.

Hunger, S., and Benning, L.G. (2007) Greigite: a true intermediate on the polysulfide pathway to pyrite. *Geochem Trans* **8**: 1.

Juniper, S.K., and Fouquet, Y. (1988) Filamentous iron-silica deposits from modern and ancient hydrothermal sites. *Can Mineral* **26**: 859–869.

Kanai, T., Imanaka, H., Nakajima, A., Uwamori, K., Omori, Y., Fukui, T., *et al*. (2005) Continuous hydrogen production by the hyperthermophilic archaeon, *Thermococcus kodakaraensis* KOD1. *J Biotechnol* **116**: 271–282.

Kashefi, K., and Lovley, D.R. (2000) Reduction of Fe(III), Mn(IV), and toxic metals at 100 degrees C by Pyrobaculum islandicum. *Appl Environ Microbiol* **66**: 1050–1056.

Kashefi, K., Tor, J.M., Holmes, D.E., Gaw Van Praagh, C.V., Reysenbach, A.L., and Lovley, D.R. (2002) Geoglobus ahangari gen. nov., sp. nov., a novel hyperthermophilic archaeon capable of oxidizing organic acids and growing autotrophically on hydrogen with Fe(III) serving as the sole electron acceptor. *Int J Syst Evol Microbiol* **52**: 719–728.

Kashefi, K. (2012) Hyperthermophiles: metabolic diversity and biotechnological applications. In *Extremophiles: Microbiology and Biotechnology*, Anitori, R.P. (ed). Norfolk, UK: Caister Academic Press, pp. 183–231.

Kashyap, S., Sklute, E.C., Dyar, M.D., and Holden, J.F. (2018) Reduction and morphological transformation of synthetic nanophase iron oxide minerals by hyperthermophilic archaea. *Front Microbiol* **9**: 1550.

Kormas, K.A., Tivey, M.K., Von Damm, K., and Teske, A. (2006) Bacterial and archaeal phylotypes associated with distinct mineralogical layers of a white smoker spire from a deep-sea hydrothermal vent site (9°N, East Pacific rise). *Environ Microbiol* **8**: 909–920.

Krause, M.O., and Oliver, J.H. (1979) Natural widths of atomic K and L levels, Kα X-ray lines and several KLL auger lines. *J Phys Chem Ref Data Monogr* **8**: 329–338.

Lasocki, S., Gaillard, T., and Rineau, E. (2014) Iron is essential for living! *Crit Care* **18**: 678.

Lin, T.J., Breves, E.A., Dyar, M.D., Ver Eecke, H.C., Jamieson, J.W., and Holden, J.F. (2014) Magnetite formation from ferrihydrite by hyperthermophilic archaea from Endeavour segment, Juan de Fuca ridge hydrothermal vent chimneys. *Geobiology* **12**: 200–211.

Lin, T.J., Ver Eecke, H.C., Breves, E.A., Dyar, M.D., Jamieson, J.W., Hannington, M.D., *et al*. (2016) Linkages between mineralogy, fluid chemistry, and microbial communities within hydrothermal chimneys from the Endeavour segment, Juan de Fuca ridge. *Geochem Geophys Geosyst* **17**: 300–323.

Little, C.T.S., and Vrijenhoek, R.C. (2003) Are hydrothermal vent animals living fossils? *Trends Ecol Evol* **18**: 582–588.

Lundin, A. (2000) Use of firefly luciferase in ATP-related assays of biomass, enzymes, and metabolites. *Methods Enzymol* **305**: 346–370.

Luther, G.W. (1991) Pyrite synthesis via polysulfide compounds. *Geochim Cosmochim Acta* **55**: 2839–2849.

Luther, G.W., Rozan, T.F., Taillefert, M., Nuzzio, D.B., Di Meo, C., Shank, T.M., *et al*. (2001a) Chemical speciation drives hydrothermal vent ecology. *Nature* **410**: 813–816.

Luther, G.W., Glazer, B.T., Hohmann, L., Popp, J.I., Taillefert, M., Rozan, T.F., *et al*. (2001b) Sulfur speciation monitored in situ with solid state gold amalgam voltammetric micro-electrodes: polysulfides as a special case in sediments, microbial mats and hydrothermal vent waters. *J Environ Monit* **3**: 61–66.

Maillot, F., Morin, G., Wang, Y., Bonnin, D., Ildefonse, P., Chaneac, C., and Calas, G. (2011). New insight into the structure of nanocrystalline ferrihydrite : EXAFS evidence for tetrahedrally coordinated iron(III). *Geochim Cosmochim Acta* **75**: 2708–2720.

Mann, S., Sparks, N.H.C., Frankel, R.B., Bazylinski, D.A., and Jannasch, H.W. (1990) Biomineralization of ferromagnetic greigite (Fe3S4) and iron pyrite (FeS2) in a magnetotactic bacterium. *Nature* **343**: 258–261.

Manzella, M.P., Reguera, G., and Kashefi, K. (2013) Extracellular electron transfer to Fe(III) oxides by the hyperthermophilic archaeon Geoglobus ahangari via a direct contact mechanism. *Appl Environ Microbiol* **79**: 4694–4700.

Matamoros-Veloza, A., Cespedes, O., Johnson, B.R.G., Stawski, T.M., Terranova, U., de Leeuw, N.H., and Benning, L.G. (2018) A highly reactive precursor in the iron sulfide system. *Nat Commun* **9**: 3125.

McCollom, T.M. (2007) Geochemical constraints on sources of metabolic energy for chemolithoautotrophy in ultramafic-hosted deep-sea hydrothermal systems. *Astrobiology* **7**: 933–950.

McGuire, M.M., Edwards, K.J., Banfield, J.F., and Hamers, R.J. (2001) Kinetics, surface chemistry, and structural evolution of microbially mediated sulfide mineral dissolution. *Geoch Cosmochim acta* **65**: 1243–1258.

Merrot, P., Juillot, F., Noël, V., Lefebvre, P., Brest, J., Menguy, N., *et al*. (2019) Nickel and iron partitioning between clay minerals, Fe-oxides and Fe-sulfides in lagoon sediments from New Caledonia. *Sci Total Environ* **689**: 1212–1227.

Miot, J., and Etique, M. (2016) Formation and transformation of iron-bearing minerals by iron(II)-oxidizing and iron(III)-reducing bacteria. In *Iron Oxides*, Faivre, D. (ed). Weinheim, Germany: Wiley-VCH Verlag GmbH & Co. KGaA.

Morin, G., Juillot, F., Casiot, C., Bruneel, O., Personné, J.-C., Elbaz-Poulichet, F., *et al*. (2003) Bacterial formation of tooeleite and mixed arsenic(III) or arsenic(V)-iron(III) gels in the Carnoulès acid mine drainage, France. A XANES, XRD and SEM study. *Environ Sci Tech* **37**: 1705–1712.

Morin, G., Noël, V., Menguy, N., Brest, J., Baptiste, B., Tharaud, M., *et al*. (2017) Nickel accelerates pyrite nucleation at ambient temperature. *Geochem Perspect Lett* **5**: 6–11.

Muehe, E.M., Morin, G., Scheer, L., Le Pape, P., Esteve, I., Daus, B., and Kappler, A. (2016) Arsenic(V) incorporation in vivianite during microbial reduction of arsenic(V)-bearing biogenic Fe(III) (oxyhydr)oxides. *Environ Sci Tech* **50**: 2281–2291.

Noël, V., Marchand, C., Juillot, F., Ona-Nguema, G., Viollier, E., Marakovic, G., *et al*. (2014) EXAFS analysis of iron cycling in mangrove sediments downstream of a lateritized ultramafic watershed (Vavouto Bay, New Caledonia). *Geoch Cosmochim Acta* **136**: 211–228.

Noël, V., Juillot, F., Morin, G., Marchand, C., Ona-Nguema, G., Viollier, E., *et al*. (2017) Oxidation of Ni-rich mangrove sediments after isolation from the sea. In *Fe and Ni Behavior and Environmental Implications*. Dumbea Bay, New Caledonia: ACS Earth and Space Chemistry. https://doi.org/10.1021/acsearthspacechem.7b00005.

Payne, D., Spietz, R.L., and Boyd, E.S. (2021) Reductive dissolution of pyrite by methanogenic archaea. *ISME J* **15**: 3498–3507. https://doi.org/10.1038/s41396-021-01028-3.

Picard, A., Gartman, A., and Girguis, P.R. (2016) What do we really know about the role of microorganisms in iron sulfide mineral formation? *Front Earth Sci* **4**: 68.

Picard, A., Gartman, A., Clarke, D.R., and Girguis, P.R. (2018) Sulfate-reducing bacteria influence the nucleation and growth of mackinawite and greigite. *Geoch Cosmochim Acta* **220**: 363–384.

Picard, A., Gartman, A., Cosmidis, J., Obst, M., Vidoudez, C., Clarke, D.R., and Girguis, P.R. (2019) Authigenic metastable iron sulfide minerals preserve microbial organic carbon in anoxic environments. *Chem Geol* **530**: 1–13.

Prieur, D., Erauso, G., Geslin, C., Lucas, S., Gaillard, M., Bidault, A., *et al*. (2004) Genetic elements of Thermococcales. *Biochem Soc Trans* **32**: 184–187.

Raiswell, R., and Canfield, D.E. (2011) The iron biogeochemical cycle past and present. *Geochem Perspect* **1**: 1–2.

Ravel, B., and Newville, M. (2005) ATHENA, ARTEMIS, HEPHAESTUS: data analysis for X-ray absorption spectroscopy using IFEFFIT. *J Synch Rad* **12**: 537–541.

Remonsellez, F., Orell, A., and Jerez, C.A. (2006) Copper tolerance of the thermoacidophilic archaeon *Sulfolobus metallicus*: possible role of polyphosphate metabolism. *Microbiology* **152**: 59–66.

Rickard, D. (1997) Kinetics of pyrite formation by the H2S oxidation of iron (II) monosulfide in aqueous solutions between 25 and 125°C: the mechanism. *Geochim Cosmochim Acta* **61**: 135–147.

Rickard, D., and Luther, G.W., III. (2007) Chemistry of iron sulfides. *Chem Rev* **107**: 514–562.

Rickard, D. (2012) Sulfidic sediments and sedimentary rocks. In *Developments in Sedimentology*, Vol. **65**. Amsterdam: Elsevier. https://doi.org/10.1126/science.207.4437.1355.

Schauder, R., and Müller, E. (1993) Polysulfide as a possible substrate for sulfur-reducing bacteria. *Arch Microbiol* **160**: 377–382.

Schicho, R.N., Ma, K., Adams, M.W.W., and Kelly, R.M. (1993) Bioenergetics of sulfur reduction in the hyperthermophilic archaeon Pyrococcus furiosus. *J Bacteriol* **175**: 1823–1830.

Scholten, L., Schmidt, C., Lecumberri-Sanchez, P., Newville, M., Lanzirotti, A., Sirbescu, M.L.C., and MacInnis, M.S. (2019) Solubility and speciation of iron in hydrothermal fluids. *Geoch Cosmo Acta* **252**: 126–143.

Schut, G.J., Boyd, E.S., Peters, J.W., and Adams, M.W. (2013) The modular respiratory complexes involved in hydrogen and sulfur metabolism by heterotrophic hyperthermophilic archaea and their evolutionary implications. *FEMS Microbiol Rev* **37**: 182–203.

Seder-Colomina, M., Mangeret, A., Stetten, L., Merrot, P., Diez, O., Julien, A., *et al*. (2018) Carbonate facilitated mobilization of uranium from lacustrine sediments under anoxic conditions. *Environ Sci Tech* **52**: 9615–9624.

Slobodkin, G.B., Kolganova, T.V., Querellou, J., Bonch-Osmolovskaya, E.A., and Slobodkin, A.I. (2009) Geoglobus acetivorans sp. nov., an iron(III)-reducing archaeon from a deep-sea hydrothermal vent. *IJSEM* **59**: 2880–2883.

Stanley, W., and Southam, G. (2018) The effect of gram-positive (Desulfosporosinus orientis) and gram-negative (Desulfovibrio desulfuricans) sulfate-reducing bacteria on iron sulfide mineral precipitation. *Can J Microbiol* **64**: 629–637.

Stetten, L., Mangeret, A., Brest, J., Seder-Colomina, M., Le Pape, P., Ikogou, M., *et al*. (2018) Geochemical control on the reduction of U(VI) to mononuclear U(IV) species in lacustrine sediment. *Geoch Cosmochim Acta* **222**: 171–186.

Sylvan, J.B., Toner, B.M., and Edwards, K.J. (2012) Life and death of deep-sea vents: bacterial diversity and ecosystem succession on inactive hydrothermal sulfides. *mBio* **3**: e00279–e00211.

Takai, K., Komatsu, T., Inagaki, F., and Horikoshi, K. (2001) Distribution of archaea in a black smoker chimney structure. *Appl Environ Microbiol* **67**: 3618–3629.

Taylor, K.G., and Konhauser, K.O. (2011) Iron in earth surface systems: a major player in chemical and biological processes. *Elements* **7**: 83–88.

Thiel, J., Byrne, J.M., Kappler, A., Schink, B., and Pester, M. (2019) Pyrite formation from FeS and H_2S is mediated through microbial redox activity. *Proc Natl Acad Sci U S A* **116**: 6897–6902.

Tivey, M.K. (2007) Generation of seafloor hydrothermal vent fluids and associated mineral deposits. *Oceanography* **20**: 50–65.

Tivey, M.K., Olson, L.O., Miller, V.W., and Light, R.D. (1990) Temperature measurements during initiation and growth of a black smoker chimney. *Nature* **346**: 51–54.

Toner, B.M., Rouxel, O.J., Santelli, C.M., Bach, W., and Edwards, K.J. (2016) Iron transformation pathways and redox micro-environments in seafloor sulfide-mineral deposits: spatially resolved Fe XAS and $\delta^{57/54}$Fe observations. *Front Microbiol* **7**: 648.

Toso, D.B., Henstra, A.M., Gunsalus, R.P., and Zhou, Z.H. (2011) Structural, mass and elemental analyses of storage granules in methanogenic archaeal cells. *Environ Microbiol* **13**: 2587–2599.

Toso, D.B., Javed, M.M., Czornyj, E., Gunsalus, R.P., and Zhou, Z.H. (2016) Discovery and characterization of iron

sulfide and polyphosphate bodies coexisting in Archaeoglobus fulgidus cells. *Archaea* **2016**: 1–11.

Turekian, K.K. (1968) *Oceans*. Prentice-Hall, Englewood: Foundations of Earth Science Series, p. 120.

Ver Eecke, H.C., Kelley, D.S., and Holden, J.F. (2009) Abundances of hyperthermophilic autotrophic Fe(III) oxide reducers and heterotrophs in hydrothermal sulfide chimneys of the northeastern Pacific Ocean. *Appl Environ Microbiol* **75**: 242–245.

Vrede, K., Heldal, M., Norland, S., and Bratbak, G. (2002) Elemental composition (C, N, P) and cell volume of exponentially growing and nutrient-limited Bacterioplankton. *Appl Environ Microbiol* **68**: 2965–2971.

Waite, T.J., Moore, T.S., Childress, J.J., Hsu-Kim, H., Mullaugh, K.M., Nuzzio, D.B., *et al*. (2008) Variation in sulfur speciation with shellfish presence at a Lau Basin diffuseflow vent site. *J Shellfish Res* **27**: 163–168.

Wang, Y.H., Morin, G., Ona-Nguema, G., and Brown, G.E. Jr. (2014) Arsenic(III) and Arsenic(V) Speciation during Transformation of Lepidocrocite to Magnetite. *Environ Sci Technol* **48**: 14282–14290.

Wilfert, P., Meerdink, J., Degaga, B., Temmink, H., Korving, L., Witkamp, G.J., *et al*. (2020) Sulfide induced phosphate release from iron phosphates and its potential for phosphate recovery. *Water Res* **171**: 115389.

Wilkin, R.T., and Barnes, H.L. (1996) Pyrite formation by reactions of iron monosulfides with dissolved inorganic and organic sulfur species. *Geochim Cosmochim Acta* **60**: 4167–4179.

Xiong, Y., Guilbaud, R., Peacock, C.L., Cox, R.P., Canfield, D. E., Krom, M.D., and Poulton, S.W. (2019) Phosphorus cycling in Lake Cadagno, Switzerland: a low sulfate euxinic ocean analogue. *Geoch Cosmochim Acta* **251**: 116–135.

Zeyen, N., Benzerara, K., Menguy, N., Brest, J., Templeton, A.S., Webb, S.M., *et al*. (2019) Fe-bearing phases in modern lacustrine microbialites from Mexico. *Geoch Cosmochim Acta* **253**: 201–230.

Zhang, L., Sun, Z.L., Geng, W., Cao, H., Qin, Y.C., Xu, C.L., *et al*. (2019) Advances in the microbial mineralization of seafloor hydrothermal systems. *China Geol* **2**: 227–237.

Supporting Information

Additional Supporting Information may be found in the online version of this article at the publisher's web-site:

Fig S1. Intracellular composition in Thermococcales cells. Intracellular composition (1) and cell observation with Cryo-EM (2) when cells are grown in medium containing native sulfur S(0) (A) or L-cystine (B). The percentages are given in weight %.

Fig S2. Production of iron sulfide minerals in S(0) condition. Scanning (A) and transmission (B, C) electron microscopy images of mineralized and aggregated cells and vesicles incubated for 144 h with mineralization medium. Scale bar: 1 μm. Cells are associated with Fe and S maps (C). The red arrows indicate the presence of greigite nanocrystals. The entirely mineralized cell labelled a, in Fig. S2B, provided the SAED pattern of pyrite of Fig. S3.

Fig S3. Electron diffraction pattern of the minerals of the cell surfaces and/or filling (providing from the cell labelled a in Fig. S2B) corresponding to pyrite. This is a polycrystalline pattern with strong preferred orientations toward a common 2–11 zone axis.

Fig S4. First stages of iron sulfides mineralization of Thermococcales in L-cystine condition. Scanning transmission electron microscopy image of the cell lysis products after 5 h of incubation in mineralization medium (A) and associated C (upper panel), P (middle panel) and Fe (lower panel). Elemental analysis by EDXS (B).

Fig S5. Presence of few non-mineralized cells after 144 h of incubation in mineralization medium in L-cystine condition. Scanning transmission electron microscopy image of single cell (indicated by black circle) close to the iron sulfide matrix (scale bar = 1 μm) and associated C (carbon panel), Fe and S maps (iron and sulfur panels).

Fig S6. Scanning electron microscopy images of abiotic controls (modified Ravot medium without cells) after 70 h of incubation in anoxic $FeSO_4$ solution (at 5 mM) in S(0) condition (A) and elemental analysis by EDX (B). Scale bar: 1 μm.

Fig S7. Scanning electron microscopy images of mineralized and aggregated cells/vesicles incubated for 192 h with mineralization medium. Scale bar = 1 μm. The intercellular/intervesicular matrix contains many greigite nanocrystals indicated by red arrows (A). The black circles indicate the presence of non-mineralized cell which separate itself from the biofilm (B).

Fig S8. ATPmetry analyses during biomineralization process. The data represent the ATP content (mM) in the sample when grown cells in sulfur (A) or in L-cystine (B) are incubated with high concentration of $FeSO_4$. For both conditions, the red curves represent the ATP level when cells are incubated with 10 mM of $FeSO_4$; the grey curves represent the ATP level when cells are incubated with 50 mM of $FeSO_4$. For L-cystine condition, the green curve represents the ATP level when cells are incubated with 25 mM of $FeSO_4$.

Appendix S1. Supporting Information